Monthly Notices of the ROYAL ASTRONOMICAL SOCIETY

MNRAS **527,** 7306–7316 (2024) https://doi.org/10.1093/mnras/stad3581
Advance Access publication 2023 November 21

The metallicity dependence of the stellar initial mass function

Tabassum S. Tanvir [1]★ and Mark R. Krumholz [1,2]

[1] *Research School of Astronomy and Astrophysics, Australian National University, Canberra, ACT 2611, Australia*
[2] *Australian Research Council Centre of Excellence in All Sky Astrophysics (ASTRO3D), Canberra, ACT 2611, Australia*

Accepted 2023 November 8. Received 2023 November 7; in original form 2023 May 31

ABSTRACT

During star formation, dust plays the crucial role of coupling gas to stellar radiation fields, allowing radiation feedback to influence gas fragmentation and thus the stellar initial mass function (IMF). Variations in dust abundance therefore provide a potential avenue by which variation in galaxy metallicity might affect the IMF. In this paper, we present a series of radiation-magnetohydrodynamic simulations in which we vary the metallicity and thus the dust abundance from 1 per cent of solar to 3× solar, spanning the range from the lowest metallicity dwarfs to the most metal-rich early-type galaxies (ETGs) found in the local Universe. We design the simulations to keep all dimensionless parameters constant so that the interaction between feedback and star-forming environments of varying surface density and metallicity is the only factor capable of breaking the symmetry between the simulations and modifying the IMF, allowing us to isolate and understand the effects of each environmental parameter cleanly. We find that shifts in the IMF with varying metallicity at a fixed surface density are smaller than the shifts in varying surface density at a fixed surface metallicity. We also find that metallicity-induced IMF variations are too small to explain the mass-to-light ratio shifts seen in the ETGs. We therefore conclude that metallicity variations are much less important than variations in surface density in driving changes in the IMF and that the latter rather than the former are most likely responsible for the IMF variations found in ETGs.

Key words: magnetic fields – radiative transfer – turbulence – stars: formation – stars: luminosity function, mass function – stars: protostars.

1 INTRODUCTION

The stellar initial mass function (IMF) is the mass distribution of stars at the point of their birth. The IMF is one of the most important distributions in astrophysics because it at least partly determines everything from chemical evolution to the strength of feedback during galaxy formation. The IMF has been found to be nearly universal in the Milky Way and its closest neighbours, which are the only locations where measurements of the IMF by direct star counting are possible (Offner et al. 2014, and references therein). A number of hypotheses have been proposed to explain this lack of variation, mostly focusing on the universality of turbulence (Padoan, Nordlund & Jones 1997; Padoan & Nordlund 2002; Hennebelle & Chabrier 2008, 2009; Hopkins 2012, 2013; Nam, Federrath & Krumholz 2021) and the stabilizing effects of stellar radiation feedback (e.g. Bate 2009, 2012; Krumholz 2011; Krumholz, Klein & McKee 2012; Guszejnov, Krumholz & Hopkins 2016; Cunningham et al. 2018) or the isothermal–adiabatic transition (e.g. Lee & Hennebelle 2018; Hennebelle, Lee & Chabrier 2019). One important outcome of these studies is that, while turbulence alone can explain why the high-mass portion of the IMF always has the same slope, some additional physical process is likely required to explain the existence of an IMF peak at a particular mass (e.g. Krumholz 2014; Guszejnov et al. 2016, 2020; Krumholz et al. 2016). This finding is particularly significant because tentative evidence has started to emerge that in the extreme star-forming environments found in early-type galaxies (ETGs), the IMF peak shifts slightly towards lower masses than the IMF peak found in the local Universe. There are multiple lines of evidence for such a shift derived from different measurement techniques – spectroscopic (e.g. van Dokkum & Conroy 2010; Spiniello et al. 2012; La Barbera et al. 2013; Conroy, van Dokkum & Villaume 2017), dynamical (e.g. Cappellari et al. 2012; Newman et al. 2017; Oldham & Auger 2018), and gravitational lensing (Treu et al. 2010; Spiniello et al. 2015) – all pointing towards at least qualitatively consistent conclusions (see Smith 2020 for a comprehensive review). There is also much more tentative evidence for the possibility that the IMF might be more bottom-light in ultra-faint dwarf galaxies (e.g. Geha et al. 2013; Gennaro et al. 2018; however, see El-Badry, Weisz & Quataert 2017 for a contrary perspective).

These observations raise the theoretical question as to which physical processes might be responsible for inducing the shift in the IMF peak in ETGs, and at least potentially in dwarfs as well. In Tanvir, Krumholz & Federrath (2022, hereafter Paper I), we performed a series of carefully controlled radiation magnetohydrodynamic (RMHD) simulations to study the role of the environment and its interaction with stellar feedback mechanisms in setting the IMF peak. We control these experiments by keeping all the dimensionless parameters constant (e.g. virial parameter, Mach

★ E-mail: tabassum.tanvir@anu.edu.au

number, and Alfvén Mach number) while altering only one other parameter so that it is easier to deduce the role of that parameter along with the feedback mechanism. In Paper I, we explored the role of surface density and showed that with increasing surface density the IMF peak shifts towards lower masses than the ones found in the Milky Way, but by less than would be expected purely from a shift in the mean Jeans mass with surface density because of the enhanced effectiveness of stellar radiation feedback in denser environments. The resulting shift in the IMF peak plausibly matches what is required to explain the mass-to-light ratios measured in ETGs.

However, in Paper I, we did not alter another potentially important parameter that differs between ETGs and other galaxies: the metallicity, and therefore dust properties. Dust matters since it is the component of the ISM that couples gas to stellar radiation. Some previous authors have conducted numerical simulations to understand how changing metallicity, and therefore changing dust abundance, might alter the IMF. For example, Bate (2019) carries out radiation hydrodynamical simulations to study the metallicity dependence of the properties of stellar populations formed at metallicities $Z = 0.01 - 3\ Z_{\odot}$, and finds that the stellar mass distribution is largely insensitive to metallicity. This result is in qualitative agreement with a number of similar, earlier numerical studies (Myers et al. 2011; Bate 2014). More recently, however, Guszejnov et al. (2022) found that the characteristic mass of a forming stellar population does vary with both metallicity and the strength of the interstellar radiation field (ISRF). They find that with a typical Galactic ISRF, lower metallicities produce a higher characteristic mass. Chon, Omukai & Schneider (2021) also studied the IMF in metal-poor environments and found that the number of low-mass stars increases with metallicity and that the mass function is top-heavy in low-metallicity environments. Sharda & Krumholz (2022) use analytical models to survey a wide range of parameter space, and find that the characteristic stellar mass is comparatively high at metallicities low enough that metal line cooling dominates, but begins to decrease with metallicity once the metallicity is high enough ($Z \gtrsim 0.01\ Z_{\odot}$) for dust–gas coupling to dominate gas thermodynamics. Bate (2023) conducts simulations taking into account how the combined effects of increasing cosmic microwave background (CMB) intensity at high redshift and variation in metallicity impact the IMF. He finds that for the CMB intensity at redshift $z = 5$, increasing metallicity increases the characteristic mass of stars.

While all these authors have studied the effects of varying metallicity, none of the previous simulations (as opposed to analytical models) have done so for the very high surface density environments that likely characterized star formation in ETGs. Following on from that in Paper I, we present a series of RMHD simulations where we explore the role of metallicity variation in setting the IMF. A critical aspect of our simulation approach is that our experiments are engineered so that, except for the one change that we make, our simulations are all simply rescaled versions of one another, such that if we were to turn off stellar feedback and complex thermodynamics, and simply adopt an isothermal equation of state, the results of all simulations would be identical. This allows us to solve the problem of interpretability since we can then unambiguously connect effects and causes.

We describe the numerical method and initial conditions we use to achieve these effects in Section 2. In Section 3, we discuss the results from our simulations and their implications for the physics behind the IMF. We summarize our conclusions in Section 4.

2 NUMERICAL METHODS AND INITIAL CONDITION

2.1 Numerical methods

The numerical methods we employ in this study are identical to those used in Paper I, and we refer interested readers to that paper for more detailed information. Here, we provide a brief summary. We carry out our simulations using the ORION2 adaptive mesh refinement code (Li et al. 2021). The code uses the approach of Li et al. (2012) to solve the equations of ideal magnetohydrodynamics (MHD) with self-gravity (Truelove et al. 1998; Klein et al. 1999) and radiation transfer (Krumholz, Klein & McKee 2007) in the two-temperature, mixed-frame, grey, flux-limited diffusion approximation.

The code includes sink particles (Krumholz, McKee & Klein 2004) to replace regions where protostars are forming and that are collapsing beyond our ability to resolve. Each sink particle runs a one-zone protostellar evolution model as described in Offner et al. (2009), which provides the instantaneous properties of the star that it represents, such as radius, luminosity, and polytropic index; these depend on the accretion history determined self-consistently from the simulations. The luminosity of each sink particle is then used as a source term in the radiative transfer equations. We also take into account the feedback caused by protostellar outflows through momentum sources around each sink particle. The outflow model we use is described in Cunningham et al. (2011). In this model, whenever mass is accreted on to a sink particle, a fraction f_w of it is ejected back into the simulation in the form of an outflow. This outflow material is launched with a speed of v_w. In our simulation, we adopt the same wind model parameters used in Hansen et al. (2012) and Cunningham et al. (2018), with $f_w = 0.3$ and $v_w = \min(v_{\rm Kep}, 60\ {\rm km\ s^{-1}})$, where $v_{\rm Kep}$ is the Keplerian speed at the protostar's surface (also determined self-consistently from the accretion history via the protostellar evolution model). These parameters are based on observations of the momentum budget of protostellar outflows (Richer et al. 2000).

A critical component of the simulations is the opacity of the dusty gas, which is responsible for coupling the gas flow to the radiation field generated by the stars and by the thermal radiation from the dusty gas itself. As in Paper I, we take the Rosseland and Planck mean opacity of the dusty gas as a function of density and temperature from the tabulated results of Semenov et al. (2003). In order to study the effects of varying the metallicity, we scale these tabulated opacities by the metallicity relative to solar, i.e. for runs with metallicity $Z = 0.1\ Z_{\odot}$, we take the opacities to be 10 per cent of Semenov et al.'s tabulated values. We should therefore understand the metallicity we quote when describing our simulations as the dust metallicity; the gas-phase metallicity is unimportant as long as the density is high enough for dust and gas to be thermally coupled by collisions since in this case dust heating and cooling completely dominates the gas thermodynamics.

2.2 Caveats

There is a limitation to the radiation transfer method: we assume that the dust and gas temperatures are equal. This is generally a good assumption for gas and dust temperatures at densities above 10^4 to $10^5\ {\rm cm^{-3}}$ (e.g. Goldsmith 2001). However, in low-density regions, dust–gas collisions may occur too infrequently to allow efficient gas–dust coupling, allowing gas to be either hotter or cooler than the dust. This is, however, unlikely to be a factor in determining the IMF since in regions where gas is collapsing and fragmenting, the

Table 1. Simulation parameters and outcomes, from left to right: run name, mass in the computational box, size of the computational box, mean density in the computational box, initial magnetic field strength, mean-density free-fall time, cell size at the finest AMR level, turbulent crossing time, surface density, metallicity, optical depth computed using the Planck mean opacity evaluated at a temperature $T = 100$ K, and number of stars formed at the times when the SFE reaches 2.5 and 5 per cent. All simulations use the same initial velocity dispersion $\sigma_0 = 2.4$ km s^{-1} and temperature $T_0 = 10$ K.

Name	$M_{\rm box}$ (M$_\odot$)	L (pc)	ρ_0 (g cm^{-3})	B_0 (mG)	$t_{\rm ff}$ (kyr)	Δx (au)	$t_{\rm cross}$ (Myr)	Σ (g cm^{-2})	$Z/Z_\odot$	τ_{100K}	$N_\star^{2.5\ \rm per\ cent}$	$N_\star^{5\ \rm per\ cent}$
L1 per cent	2000	0.92	1.74×10^{-19}	0.36	160	46	0.4	0.5	0.01	5.38×10^{-3}	185	290
L10 per cent	2000	0.92	1.74×10^{-19}	0.36	160	46	0.4	0.5	0.1	0.054	182	299
L1×	2000	0.92	1.74×10^{-19}	0.36	160	46	0.4	0.5	1	0.54	204	319
L3×	2000	0.92	1.74×10^{-19}	0.36	160	46	0.4	0.5	3	1.6	190	291
M1 per cent	1000	0.46	6.96×10^{-19}	0.73	80	23	0.2	1	0.01	0.0108	174	267
M10 per cent	1000	0.46	6.96×10^{-19}	0.73	80	23	0.2	1	0.1	0.108	220	324
M1×	1000	0.46	6.96×10^{-19}	0.73	80	23	0.2	1	1	1.08	224	336
M3×	1000	0.46	6.96×10^{-19}	0.73	80	23	0.2	1	3	3.2	220	314

density is high enough for gas and dust to be well coupled. Studies that have treated gas and dust temperatures separately find that its effect on fragmentation is minimal (Bate 2019). In our simulations, we also have not considered how metallicity might affect early stellar evolution and therefore jet formation. We do not include any ISRF in our simulations, so how metallicity variation might affect the temperature distribution of the gas without the presence of a protostar is also absent from our simulations.

2.3 Initial and boundary conditions

We construct our initial conditions following Paper I, and we refer readers to that paper for full details. Our initial conditions are designed to produce a carefully controlled experiment, whereby we hold all simulation parameters fixed except for one, which we vary systematically in order to isolate the effects of that parameter. In this study, we consider two different series of runs. The *medium*-density case (M runs hereafter) consists of a periodic box[1] containing a mass $M_{\rm box} = 1000$ M$_\odot$ with surface density $\Sigma = 1$ g cm^{-2} (corresponding to a mean density $\rho_0 = 7.0 \times 10^{-19}$ g cm^{-3} and box length $L = 0.46$ pc), an initial temperature $T_0 = 10$ K, an initial gas velocity dispersion $\sigma = 2.4$ km s^{-1}, and an initially uniform magnetic field of strength $B_0 = 0.73$ mG; for this combination of parameters, the box free-fall time $t_{\rm ff} = 80$ kyr, the crossing time $t_{\rm cross} = 0.4$ Myr, the virial ratio $\alpha_{\rm vir} = 5\sigma_v^2 L/3GM_{\rm box} = 1$, the Mach number $\mathcal{M} = 12.6$, and the plasma $\beta = 0.012$. The *low*-density series (L runs hereafter) is a rescaled version of the M runs with a surface density that is lower by a factor of $f = 1/2$, and a box length, volume density, and magnetic field strength that are multiplied by factors of f^{-1}, f^2, and f relative to the M series, respectively; the gas velocity dispersion and temperature are unchanged. These transformations have the property that they leave $\alpha_{\rm vir}$, $\mathcal{M}$, and β unchanged between the L and M series, so the *only* dimensionless number that varies between the L and M series is the optical depth of the gas.

In addition to varying surface density and thus the optical depth at fixed metallicity, as in Paper I, in this study we also vary the metallicity independently of the surface density. The metallicity range we explore is from 1 per cent of solar to 3× solar; this covers the range from the lowest metallicity dwarf galaxies in the local Universe (Madden et al. 2013) to the most metal-rich early types (Gu et al. 2022). We carry out runs at $Z/Z_\odot = 1$ per cent, 10 per cent, 1, and 3 for both the L and M cases; we refer to these runs as L1 per cent, L10 per cent, L1×, and L3×, and similarly for the M series, and we summarize their full properties in Table 1. Note that the L1× and M1× runs are identical to the L1 and M1 runs in Paper I.

Metallicity variation will change how the gas interacts with stellar radiation feedback since metals (in the form of dust grains) are what couple the radiation to the gas. They will also change how the gas interacts with protostellar outflow feedback, since outflows shock the gas, and the rate at which the gas is then able to cool back down to its equilibrium temperature depends on the box's optical depth. By comparing to the solar metallicity runs reported in Paper I, we can further separate the effects of metallicity and surface density.

[1]While all MHD quantities use periodic boundaries, the radiation field uses Marshak boundaries, with an inward radiation flux corresponding to that of an isotropic blackbody radiation field with a radiation temperature of 10 K (see Paper I for full details).

2.4 Resolution, refinement, and sink particles

In order to ensure that we can compare our current runs to those carried out in Paper I, we use identical resolution, refinement, and sink particle creation criteria, and we refer to that paper for a detailed description, which we only summarize briefly here. The adaptive mesh refinement (AMR) hierarchy in these simulations is set on a 512^3 base grid, which we denote by $\mathcal{L} = 0$.The simulation takes place in two stages; during the first, 'driving' phase, which lasts for two crossing times, we disable self-gravity and radiation transport, and drive the turbulence to a steady velocity dispersion, providing time for the turbulence to achieve a statistically steady state. During the driving phase, we disable AMR, so no higher level exists. After the driving phase, we start the 'collapse' phase, during which we disable driving and re-enable self-gravity and radiation. Once we turn on gravity, the grid is allowed to adaptively refine to a maximum level $\mathcal{L}_{\rm max} = 2$, and we refine in any cell where the Jeans number

$$J = \sqrt{\frac{G\rho\Delta x^2}{\pi c_s^2}} \tag{1}$$

rises above $J = 1/8$; here, ρ is the gas density, Δx is a cell size, and c_s is the gas isothermal sound speed. We report the size of the cells on the finest level in Table 1.

Sink particle formation is triggered in any zone on the finest AMR level where the gas is dense enough to reach a local Jeans number $J > 1/4$. Once a sink particle is formed, it interacts with the gas via gravity, accretion, and stellar feedback only.

3 RESULTS

We present the results of our simulations here. First, we give an overview of the simulations in Section 3.1. Next, we discuss the mass distribution of the sink particles and identify how different

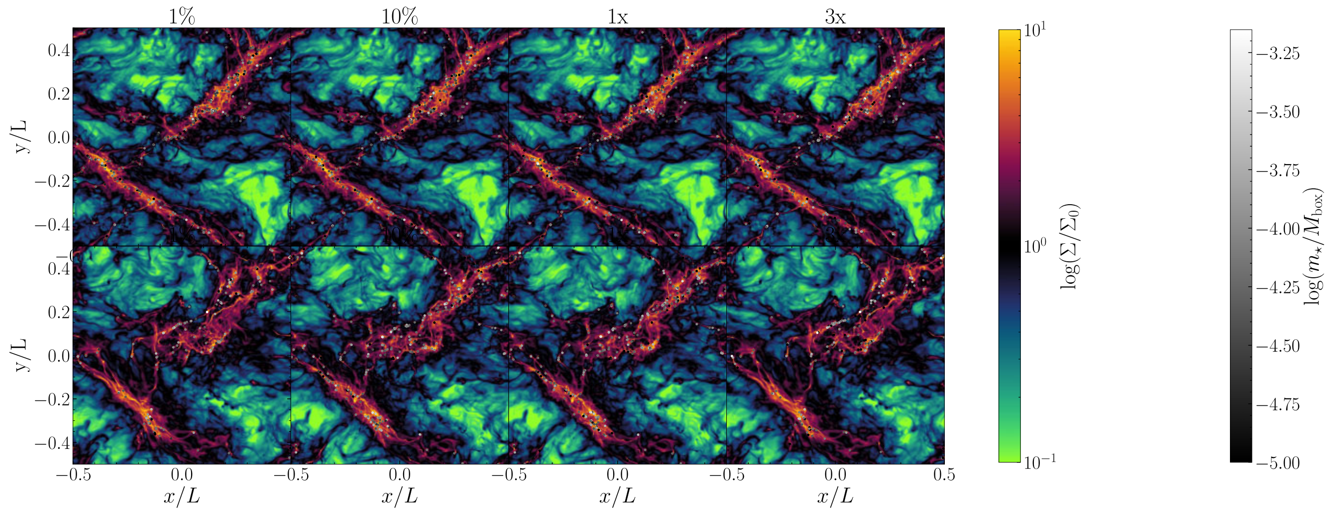

Figure 1. Column densities of simulations L (top) and M (bottom) series at 5 per cent SFE at metallicities 1 per cent, 10 per cent, 1×, and 3× solar metallicity. The colour scale goes from $\log(\Sigma/\Sigma_0) = -1$ to 1, where $\Sigma_0 = \rho_0 L$ and ρ_0 is the mean density in the simulation domain. Circles show star particles, and are colour-coded by mass $m_\star$ from $\log(m_\star/M_{\rm box}) = -5$ to -3, where $M_{\rm box}$ is the total mass of the simulation box.

metallicity at a fixed surface density impacts the IMF in Section 3.2. In Sections 3.3 and 3.4, we interpret these results in terms of the effects of radiation and protostellar outflow feedback, and the interaction of these two feedback mechanisms with gas of varying metallicity.

3.1 Overview of simulations

In Figs 1 and 2, we show the column density and the density-weighted temperature of runs L and M for our four different metallicities: 1 per cent, 10 per cent, 1×, and 3× solar metallicity. As in Paper I, we show these plots at matching star formation efficiency (SFE) instead of at matching times since star formation occurs at different times in these runs. It is clear from Fig. 1 that turbulence has created dense filamentary structures and that star formation activity is confined within these structures. Morphologically, the runs are very similar to one another, which is not surprising since by construction in the absence of a feedback mechanism these runs would be identical. There is one small difference visible between the two sets of runs with different column densities: run L produces a filamentary structure that is more straight and narrow than the filamentary structures produced in run M. By contrast, at different metallicities but fixed surface density, the simulations are almost identical to one another. This indicates that, at least with regard to morphology, metallicity has a relatively minor impact.

The temperature structure of the gas shown in Fig. 2 behaves quite differently. Here, differences with metallicity are much more apparent than in Fig. 1. For both the L and M series, lower metallicity runs are warmer compared to the higher metallicity runs. This is due to two effects: first, in the lower metallicity runs stellar radiation is able to escape further from the dense regions around individual stellar sources, leading to more widely distributed heating and a warmer mean temperature over most of the volume. Secondly, the low-metallicity runs are less efficient at radiating away the energy released in shocks than the high-metallicity runs due to their lower emissivity, an effect that likely dominates in low-density gas far from stellar sources. Both these effects favour a warmer mean temperature in the low-metallicity runs. This is in contrast to the effects of surface density, in which lower surface density runs are cooler because radiation is trapped less efficiently in the full simulation box.

We show the time evolution of the SFE in Fig. 3, and the total number of stars present as a function of the SFE in Fig. 4; we define the SFE as the ratio of total stellar mass in the simulation to the total initial mass present in the volume. We also report numerical values for the number of stars formed at 2.5 and 5 per cent SFE in the final two columns of Table 1. We find that, in all runs, once the star formation activity begins it takes approximately 0.5 free-fall times to reach 5 per cent SFE. There is very little difference between the runs with varying metallicities at a fixed surface density. This indicates that whatever effects the feedback mechanisms have on the star formation rate in the simulations are independent of metallicity and surface density. By contrast, we see larger differences in Fig. 4, which shows the number of stars as a function of SFE. Although the results are noisy and the trend is weak, there is none the less a clear trend in both the figure and the numerical values provided in Table 1. At essentially all SFEs for a given surface density, the run with the smallest number of stars is one of the runs at 1 or 10 per cent of solar metallicity (i.e. L1 per cent or L10 per cent from the L series, and M1 per cent or M10 per cent from the M series), while the run with the largest number of stars present is one of the runs with solar or 3× solar metallicity (L1× or L3× from the L series, and M1× or M3× from the M series). In general, we see that at almost all SFEs the higher metallicity runs on average have more stars than the two lower metallicity ones, indicating that the stars formed in these runs have systematically lower masses. However, while this is true in our simulations, we caution that because the effect is very weak in reality it might be overwhelmed by other physical processes that occur below our resolution limit or that are otherwise omitted from our simulations. None the less, we examine these trends further in the next section, for the purpose of understanding their origin in the physics that we do capture.

3.2 Stellar mass distribution

To explore the metallicity dependence of the stellar mass function further, we present two sets of plots. The first, Fig. 5, shows the evolution of the median of the sink particle mass distributions for all

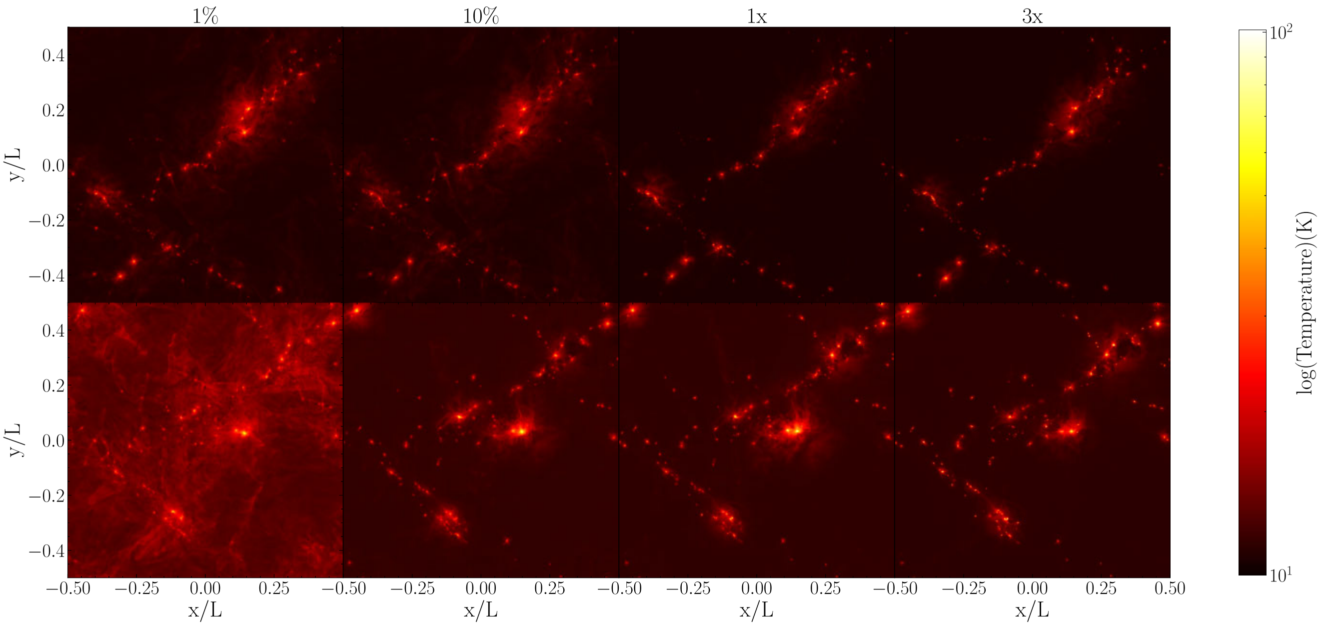

Figure 2. Same as Fig. 1, but showing density-weighted projected temperature rather than column density.

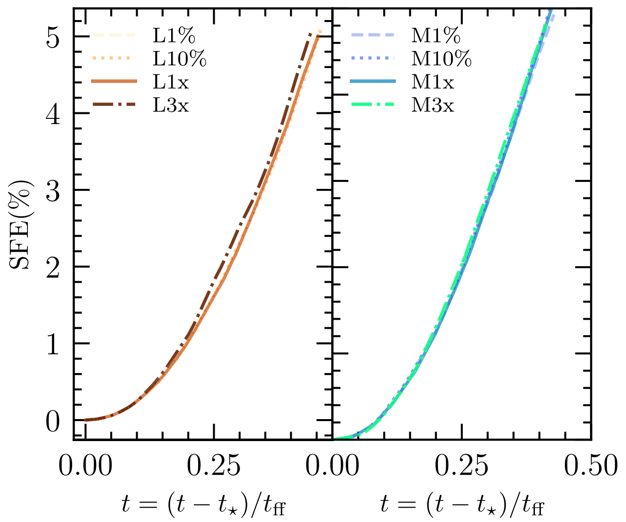

Figure 3. SFE as a function of time since the formation of the first star $t_\star$, measured in units of the free-fall time $t_{\rm ff}$. The left panel shows the L series of runs at different metallicities, and the right panel shows the corresponding results for the M series.

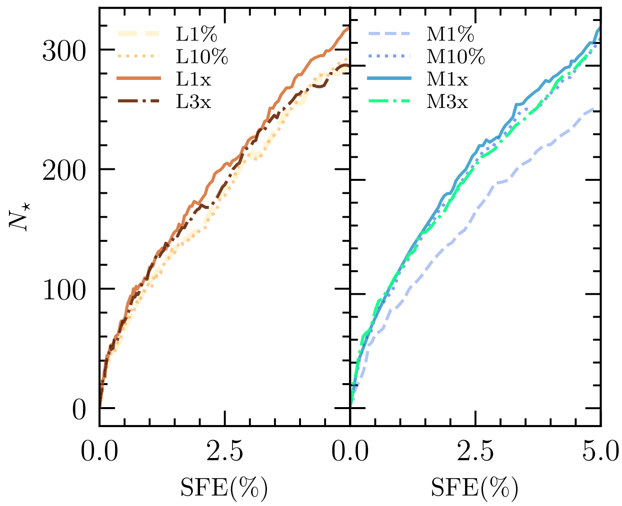

Figure 4. Number of stars formed as a function of SFE. As in Fig. 3, the left panel shows the L run series and the right panel shows the M series.

the runs. As in Paper I, we measure the median with respect to the stellar mass rather than the number, i.e. the median stellar mass m_* is defined by the condition that half the total stellar mass is found in stars with masses $<m_*$. Looking at Fig. 5, we see that the median masses have reached nearly steady values at 5 per cent SFE. When measured on both absolute (top panel) and relative scales (bottom panel), the L runs at varying metallicity show greater variation in median mass than the M runs; however, the direction of variation is the same in both sets of runs, which is that as the metallicity increases the median mass decreases. However, we further note that the differences between the different metallicities are smaller than the differences between runs L and M, particularly when expressed in terms of absolute rather than relative mass.

To investigate these differences further, in Fig. 6 we show the cumulative mass functions of the runs at 5 per cent SFE on both absolute and relative mass scales; as in Fig. 5, we measure the cumulative distribution function (CDF) with respect to mass rather than number, since this is much more numerically stable. Consistent with the trend as a function of time shown in Fig. 5, in the L runs as the metallicity increases there is a slight shift in the CDF shape and mass range it covers, with metal-poor runs showing slightly heavier mass distributions than metal-rich runs at the high-mass end. The trend is less visible, and may in fact reverse, at the lowest stellar masses, so that the metal-rich distribution is narrowest. The variations in run M are similar to or perhaps smaller than those in run L, and are in qualitatively the same direction. Consistent with Paper I, we also see that, on an absolute scale, the L runs have a heavier IMF than the M runs. However, compared to Jones & Bate (2018), we do find a stronger effect of surface density on the IMF. This is due to a number

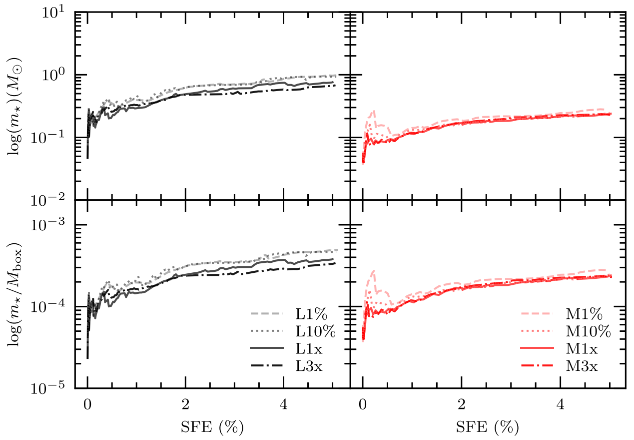

Figure 5. The top panels show the evolution of the median of the sink particle mass distributions for runs L (left) and M (right) at different metallicities in absolute mass expressed in $M_\odot$. The lower panel shows the evolution relative to the box mass $M_{\rm box}$. Here, the medians are calculated with respect to mass rather than number.

of differences in the initial conditions and physics involved in the two studies. Jones & Bate (2018) studied a non-magnetized globally collapsing cloud, whereas in this study we examine a turbulent and magnetized periodic box. Jones & Bate (2018) also did not include protostellar outflow in their simulations and because of these large differences in the set-up of the simulations it is difficult to examine which differences led to the different outcomes.

3.3 The effect of radiation feedback at varying metallicity

Recall that our simulation series is constructed so that if the gas were isothermal and not subject to protostellar feedback, the different metallicity and surface density runs would all simply be rescaled versions of the same simulation, and we would therefore expect identical results. Thus, the differences in IMF we have observed between the runs must be a result of feedback, and variations in IMF at fixed surface density must be due to the interaction of feedback with the gas of varying metallicity. In this section, we examine how radiation feedback alters gas temperature distribution in runs of varying metallicity and how this, in turn, influences fragmentation, and in the next section, we perform a similar exercise for protostellar outflow feedback.

Fig. 7 shows the gas mass distribution with respect to both density and temperature in runs L and M at different metallicity, all at 5 per cent SFE. From the plot, it is clear that there are differences between the metal-poor and the metal-rich runs. At lower densities, the metal-poor runs are clearly systematically warmer, an effect that, as noted above, is likely due to their less efficient cooling. However, the more significant differences are in the high-density parts of the distribution since this is the gas that is closest to star formation and thus whose fragmentation will most directly affect the IMF. In the metal-poor runs, we see an upturn in the minimum temperature of the dense gas, while in the more metal-rich runs the temperature remains flat as high density. The most extreme case here is the M run at 1 per cent of solar metallicity, where there is essentially no gas at densities $>10^3\rho_0$ and temperatures $\lesssim$15 K. On the other hand, the temperature distribution at high density extends to noticeably higher temperatures in the metal-rich runs than in the metal-poor ones, most likely for the same reason: because when the gas is more opaque, radiation is more easily 'bottled up', leading to hotter warm

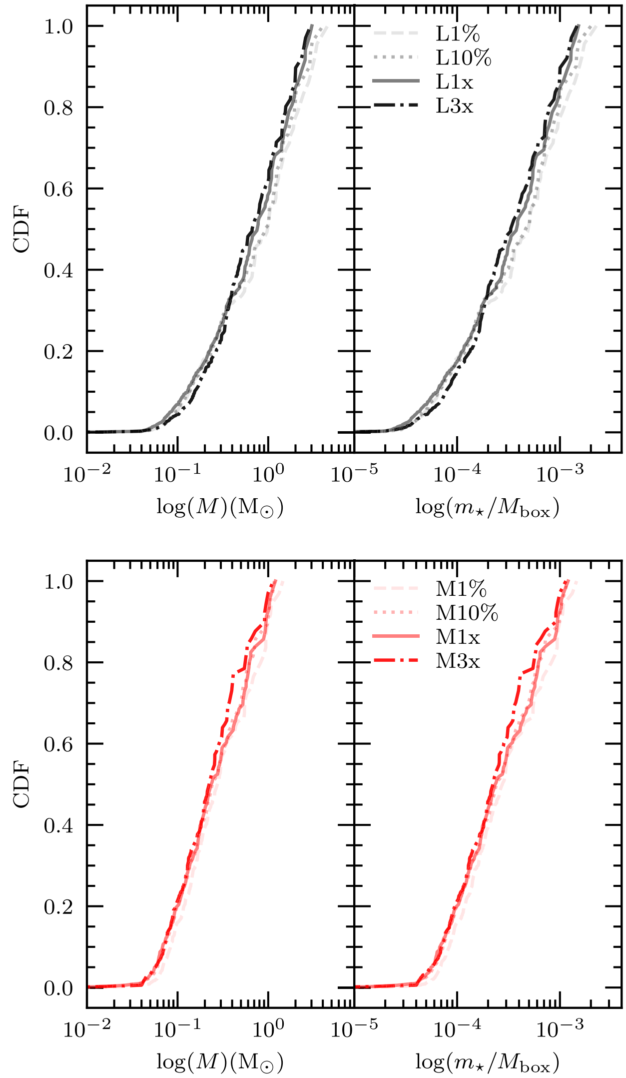

Figure 6. CDF of the sink particle masses of the simulations: the top panel is the run L at different metallicities, and the bottom panel is the run M at different metallicities. The left side is the CDF with respect to absolute stellar mass and the right side is the CDF for mass measured relative to the box mass $M_{\rm box}$. In both the L and M series, lower metallicity runs produce a slightly top-heavy IMF than the higher metallicity runs.

regions around protostars that have already started radiating. While all of these temperature differences might seem minor, recall that the Jeans mass varies as $T^{3/2}$, so a factor of 1.5 corresponds to a factor of 1.8 in mass – comparable to or larger than the IMF shifts we have observed between the runs, and of roughly the size required to explain the observations of ETGs.

In order to understand how the opacity affects fragmentation more directly, we show in Fig. 7 the 1D mass-weighted CDF of mass with respect to $M_{\rm J}/M_{\rm box}$, where $M_{\rm J}$ is the Jeans mass computed from the local gas density and temperature. For a detailed description of how to construct this figure, we refer readers to Paper I, but to summarize, note that the horizontal axis in Fig. 8 corresponds to the dashed lines of constant $M_{\rm J}/M_{\rm box}$ in Fig. 7. The vertical axis in Fig. 8 then shows what fraction of the mass in the simulation lies to the right of the corresponding dashed line in Fig. 7, i.e. it shows that fraction of the mass in a given simulation has a Jeans mass smaller than the indicated value, and thus has the potential to fragment to

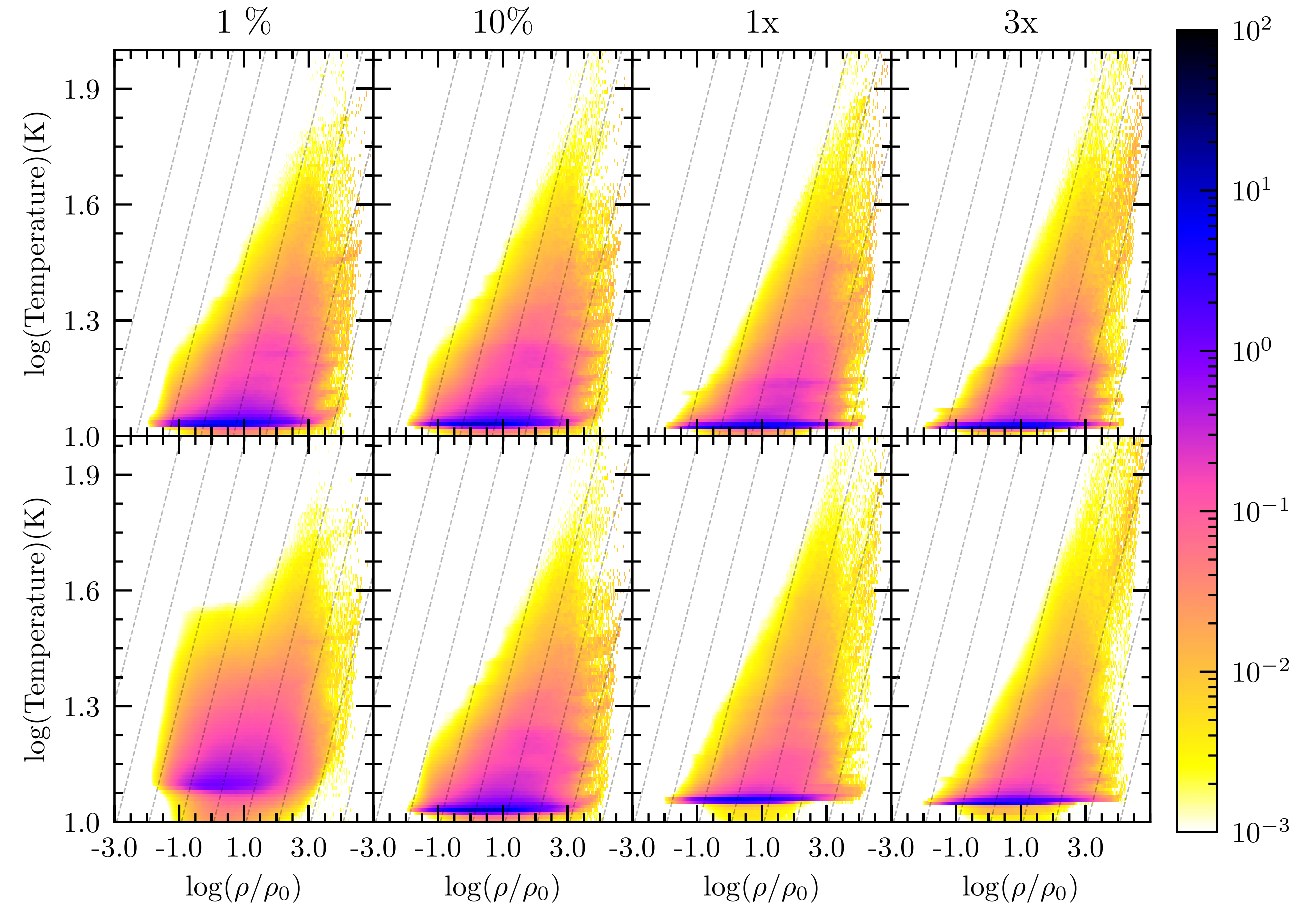

Figure 7. The joint distribution of normalized density ρ/ρ_0 and temperature T for runs L and M at different metallicity. The top row shows the state of the L runs and the bottom row shows the M runs; metallicity varies from 1 per cent to 3× solar from left to right, as indicated above the columns. All plots show the state of the simulations when they reach 5 per cent SFE. The colour bar shows the mass in each density–temperature bin. Dashed lines indicate loci of constant box-normalized Jeans mass M_J/M_{box}; lines are spaced logarithmically at intervals of 0.5 dex, with the leftmost line corresponding to $\log M_J/M_{box} = -2$.

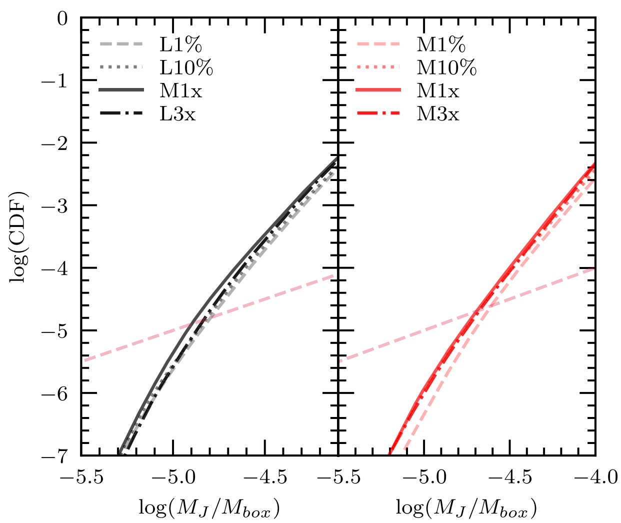

Figure 8. CDFs of mass with respect to M_J/M_{box} for the L run series (left) and the M run series (right). The dashed straight lines in each panel show the one-to-one relation, and indicate a minimum condition for fragmentation: for any mass M_J/M_{box} for which the CDF falls below the dashed line, there is less than a single Jeans mass of material with M_J that small in the box, and thus it is impossible to create an object of that mass via gravitational collapse.

produce stars with mass smaller than that value. From this plot, we see a clear trend between the metal-poor and metal-rich runs. The metal-rich runs tend to have a more mass at lower M_J/M_{box} than the metal-poor runs, consistent with our observation that the metal-rich runs produce a more bottom-heavy IMF. The location at which the dashed 1–1 line in the figure intersects the CDF gives a rough estimate of the minimum object mass that is possible for gravity to produce: to the left of this intersection point, the box contains less than a single Jeans mass of material for which M_J is that small, and is therefore not capable of producing collapsed objects of such small mass. The intersection point is on average shifted to slightly lower mass at higher metallicity, indicating that radiation feedback is more efficient in metal-poor runs at suppressing the formation of lower mass objects.

3.4 The effect of outflow feedback

As discussed in Paper I, radiation and outflow feedback play complementary roles in shaping the IMF: the former sets a lower bound on the masses of stars that can form, shaping the low-mass end of the IMF, while the latter inhibits the accumulation of mass by the most massive stars, shaping the high-mass end of the IMF. This difference explains why it is possible for the low-mass and high-mass parts of the CDF to shift in opposite directions, as we observe

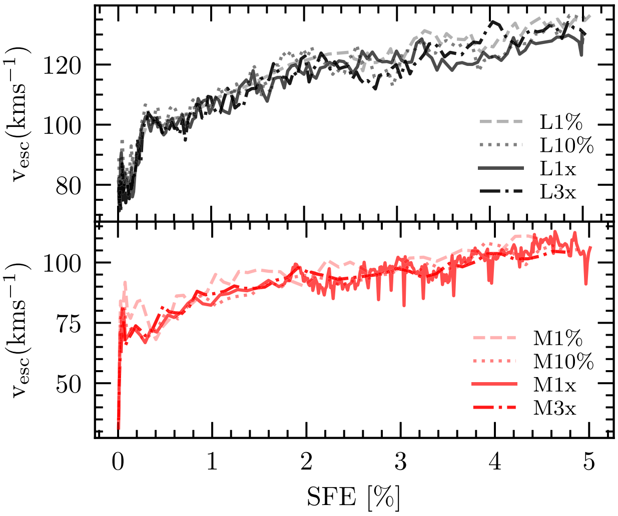

Figure 9. Accretion rate-weighted mean surface escape speed of stars formed in the simulations as a function of SFE. The top panel shows the L series of runs at varying metallicity, and the bottom panel shows the M series.

in Fig. 6. In this case, if radiation feedback were the only actor in our simulations, then we would expect a uniform shift of the IMF towards the higher masses in the metal-poor runs. The actual pattern of IMF shift with metallicity is more complex, indicating that protostellar outflow feedback is significant as well, and that its dependence on metallicity is not identical to that of radiation feedback.

To understand how outflow feedback affects our runs, we first look at Fig. 9, which shows the evolution of accretion rate-weighted mean surface escape speed in the runs as a function of SFE. This quantity matters because the outflow prescriptions we use in these simulations link the outflow velocity to the stellar surface escape speed, as is observed to be the case (Richer et al. 2000, and references therein) and as is expected theoretically (Konigl & Pudritz 2000, and references therein), since outflows are launched from close to the stellar surface (see Cunningham et al. 2011 for a detailed description of our outflow prescription). From the plot, it is clear that $v_{\rm esc}$ varies with surface density (run L has a higher surface escape speed than run M) but for a fixed surface density there is no systematic difference in the surface escape speed between the different metallicity runs; this is not surprising, given that the primary determinant of escape speed is the ratio of the time stars have had to contract towards the main sequence to the stellar Kelvin–Helmholtz time-scale; the former depends on surface density but not on metallicity (since the simulation star formation rates are almost independent of metallicity), and the latter to good approximation depends on neither. Thus, we find that at any given metallicity the L series of runs has higher mean escape speed than the M series, since the L runs take longer to reach a given SFE, but that there is no difference with metallicity.

Thus, the differences we find in how outflows influence the IMF at different metallicity cannot be a result of differences in the outflow strength. Instead, in order to understand how protostellar outflows are breaking the symmetry in the simulations, we next examine Fig. 10, which shows the total kinetic energy, scalar momentum, and volume occupied by outflow material normalized to the box kinetic energy ($E_{\rm box} = M_{\rm box}\sigma_v^2/2$, where σ_v is the initial 3D velocity dispersion), scalar momentum by $p_{\rm box} = M_{\rm box}\sigma_v$, and volume $V_{\rm box} = L^3$, respectively; we identify outflow material by a passive scalar that we add to the gas launched into outflows, and refer readers to Paper I for details on the procedure. Looking at this plot, we

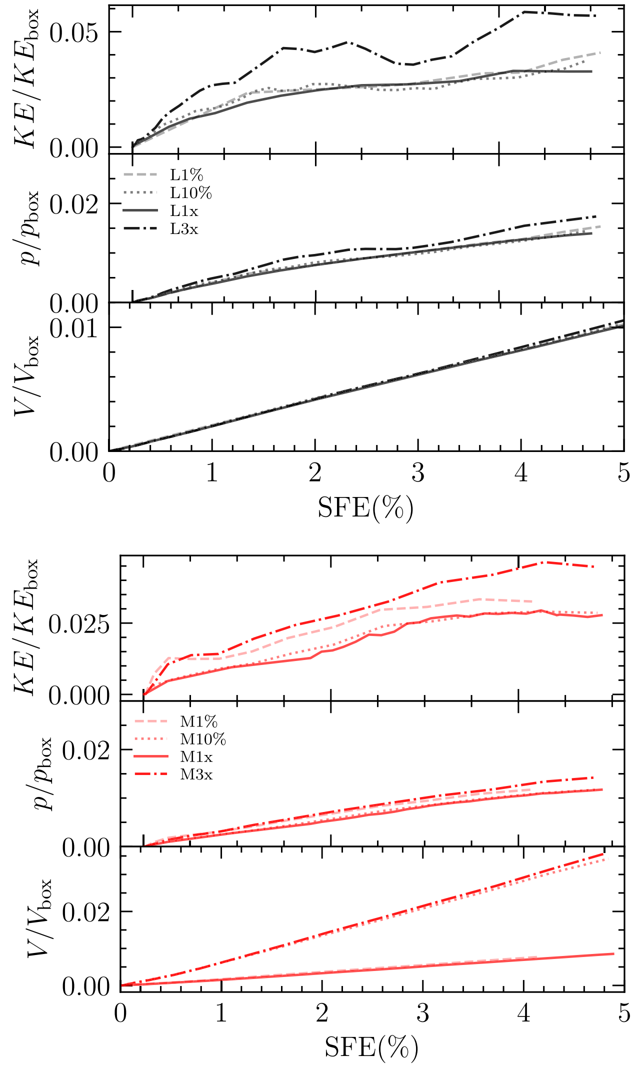

Figure 10. Outflow kinetic energy, momentum, and volume relative to the box kinetic energy, momentum, and volume, respectively, all as a function of SFE. The top set of panels shows the L series of runs and the bottom shows the M series.

see that in the metal-rich runs the outflowing material on average has more kinetic energy and scalar momentum, and occupies more volume, than for the more metal-poor runs at the same surface density. In Paper I, we found that greater outflow momentum results in *less* efficient fragmentation of the gas, because the outflows punch through their environments and escape more efficiently, therefore creating an environment more favourable to the formation of higher mass stars. However, this does not appear to be the case here: the metal-rich runs have more outflow momentum and kinetic energy, but have slightly *fewer* massive stars, as can be seen by examining the CDFs shown in Fig. 6. One possible explanation is that the outflow momentum and kinetic energy vary between the L and M run series for different reasons than they vary with metallicity at fixed surface density. The outflow energy and momentum are larger in the L runs than the M ones because the L runs have more powerful outflows due to the higher surface escape speeds achieved by stars that have longer to contract towards the main sequence. By contrast, the differences between the runs at different metallicities are almost certainly driven by the different cooling rates of the outflow gas and the dense cloud

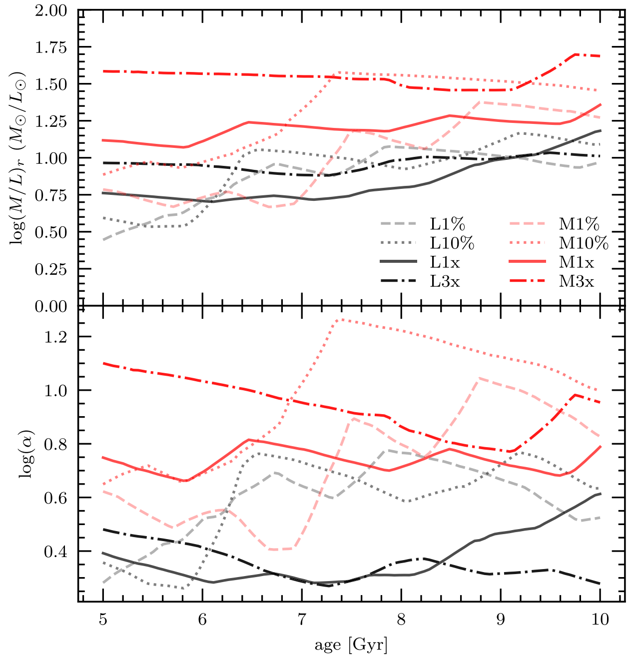

Figure 11. The top panel shows the mass-to-light ratio $(M/L)_r$ in the SDSS r band as a function of population age computed for the stellar population formed in each of the simulations, using isochrones computed with the same metallicity as used in the simulations. The black lines represent the L series of runs and the red lines represent the M series of runs, respectively, with different line styles corresponding to different metallicity as indicated in the legend. The bottom panel shows the IMF mismatch parameter $\alpha = (M/L)/(M/L)_{Z_\odot,\mathrm{Chabrier}}$, where $(M/L)_{Z_\odot,\mathrm{Chabrier}}$ is the mass-to-light ratio expected for a solar metallicity stellar population with a Chabrier (2005) IMF, again as a function of stellar population age.

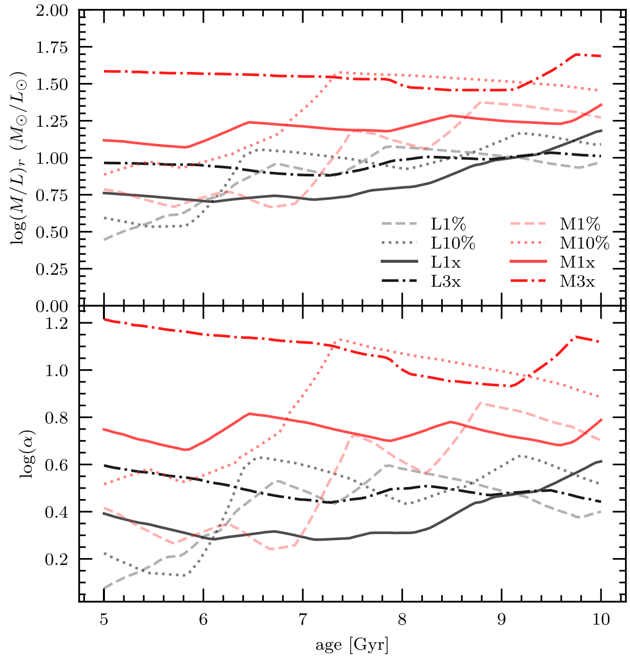

Figure 12. Same as Fig. 11, but now computed using the same set of isochrones (corresponding to those for $Z = Z_\odot$ for all simulations), regardless of the simulation metallicity.

material with which it mixes. In the metal-poor runs, cooling times are longer due to the lower metal content of the gas, and as a result, regions of shocked cloud gas may build up that pressure-confine the outflow more effectively, in turn making outflows less efficient at breaking up the gas clumps. This allows slightly more massive stars to form at the high-mass end of the IMF, as we observe in Fig. 6.

3.5 Implications for the mass-to-light ratio in early-type galaxies and local star-forming galaxies

One of the primary motivations of this study is to investigate the role of metallicity in the variations of the IMF that have been observed in ETGs. The mass-to-light ratio is the most direct line of evidence we can collect from our simulations to study these variations. In this section, we explore the mass-to-light ratios of our simulations with varying metallicity. We use the SLUG stellar population synthesis code (da Silva, Fumagalli & Krumholz 2012; Krumholz et al. 2015) to generate isochrones at stellar population ages of 5–10 Gyr and at the metallicities used in the simulations (see Paper I for a detailed description of the procedure). We use the isochrones to calculate the mass-to-light ratio of the stellar populations formed in our simulations at ages of 5–10 Gyr in the Sloan Digital Sky Survey (SDSS) r band, which is commonly used for measurements of M/L in ETGs.

The top panel of Fig. 11 shows the mass-to-light evolution of the runs from age 5–10 Gyr, while the lower panel shows the IMF mismatch parameter α, defined as the ratio of the actual M/L ratio in the simulations to the M/L ratio expected for a population with a solar metallicity and a Chabrier (2005) IMF at the same age; this latter quantity is the index most commonly used in observations to study IMF variations in ETGs, though we emphasize that the absolute value here is less significant than the differences between the runs due to the systematic uncertainties. For both the absolute M/L or the IMF mismatch parameter, we see that, at any given metallicity, there is a difference of ∼0.3–0.5 dex in mass-to-light ratio between the L and M runs; this finding is consistent with that in Paper I for the solar metallicity case, and extends the results to non-solar metallicities. At a fixed surface density, by contrast, there is a smaller difference in the mass-to-light ratio between the runs, consistent with our finding that surface density is a more influential factor than metallicity when it comes to determining the IMF.

Moreover, Fig. 11 in fact somewhat exaggerates the effect of metallicity, because some of the difference in mass-to-light ratio between the differing metallicity runs occurs because the metallicity itself affects stellar evolution and atmospheres; thus, we would not expect two identical M/L values for two populations of different metallicity even if they had exactly the same IMF. To remove this effect, in Fig. 12 we show the same quantities as in Fig. 11, but where we have calculated the mass-to-light ratio for all runs using the isochrones for solar metallicity; while this is clearly artificial, it enables us to isolate the effects of metallicity on the IMF from the effects on stellar evolution and atmospheres. In Fig. 12, the runs at different metallicity but the same surface density cluster even more tightly, and are further from the corresponding runs at different surface density, than in Fig. 11. This reinforces our conclusion that the effects of metallicity on the IMF and the observational diagnostics used to assess it are fairly minor compared to the effects of surface density.

Our qualitative conclusion that metallicity effects cannot be responsible for the IMF variations seen in ETGs is the same as that reached in a recent paper by Bate (2023), who explored the role of varying metallicity on the stellar properties at redshift $z =$ 5. Bate found that at this redshift, with its higher CMB temperature, increasing metallicity leads to an increase in the characteristic mass of stars, exactly the opposite of what would be required to reproduce observed IMF variations in ETGs. However, our conclusions differ somewhat in detail; Bate varied both the metallicity and the CMB temperature, whereas we, in keeping with our philosophy of controlled experiments, have varied only the former, a decision that is likely to be significant at $z \gtrsim 3$, when the CMB temperature begins to exceed our adopted background infrared radiation field temperature of 10 K. Thus, there is no contradiction between the findings of Bate (2023) and of this work, since the experiments we have carried out are different. On the other hand, our finding that there is a very weak IMF variation with metallicity at fixed surface density is qualitatively consistent with the findings of Bate (2019), though they explore only a single surface density case, one similar to our L series.

It is also interesting to consider the implications of our findings for variations within individual galaxies, including the Milky Way. In the local Universe, star-forming galaxies typically have metallicity gradients of ~ -0.1 dex per effective radius or shallower (e.g. Mingozzi et al. 2020), implying variations within galaxies that are substantially smaller than those between galaxies; since even the latter have proven to be relatively unimportant, the former are likely to be as well.

On the other hand, surface densities plausibly vary more within galaxies, and thus our results might seem to imply that there should be substantial IMF variations within the Milky Way or in other nearby galaxies, which are not observed (see Section 1). Here, however, we encounter a limitation of our idealized simulation methodology: while the surface density is defined unambiguously in our simulations, and in other simulations that begin from either periodic boxes or isolated clouds, real star-forming clouds do not have sharp edges that admit an unambiguous definition of surface density. While it is clear that no matter what definition is adopted there will be large differences in surface density between the early starbursts that are the likely progenitors of ETGs and local spirals, this is not true for variations within spirals. For example, if we consider the surface density of molecular gas as traced by CO, Faesi, Lada & Forbrich (2018) find no systematic correlation between surface density and galactocentric radius for 10 pc-scale measurements in NGC 300, while Sun et al. (2020) find substantial covariance at $\gtrsim$100 pc scales in a larger galaxy sample. It is unclear as to which of these, if either, is the 'right' surface density to map on to our idealized simulations. Thus, we are not currently in a position to make strong claims regarding IMF variations within single galaxies. Addressing this question will likely require multiscale simulations that zoom in from galactic scales down to the smaller scales where our simulations begin.

4 CONCLUSIONS

In this paper, we present a set of RMHD simulations of star formation including radiation and protostellar outflow feedback from young stars. We carry out a systematic exploration of how the mass function of the stars formed in the simulations varies as a function of surface density and metallicity, exploring surface densities from those typical of Milky Way-like galaxies to those typical of starbursts or ETGs, and metallicities that range from those typical of the most metal-poor local dwarfs, $Z = \mathrm{Z}_{\odot}/100$, to those typical of the centres of the most metal-rich early types, $Z = 3\,\mathrm{Z}_{\odot}$. The set-up of the simulations allows us to separate out the effects of metallicity at fixed surface density and of surface density at fixed metallicity, and to identify the specific mechanisms by which these parameters interact with stellar feedback. This extends the results of Paper I, which used the same methodology to explore the effects of surface density alone, without metallicity variation.

Overall, we see a trend whereby metal-poor cases produce a slightly heavier mass distribution over most of the IMF than metal-rich cases. However, this trend disappears or reverses at the lower mass end of the IMF, so that metal-rich cases also have a slightly narrower IMF overall. We attribute these shifts to the contrasting ways in which metallicity variation interacts with different types of stellar feedback. This high-mass end of the IMF is sensitive primarily to the effects of protostellar outflow feedback inhibiting the most massive objects from accreting, something that appears to happen slightly more efficiently when the metallicity is higher and cooling of outflow-shocked gas is more rapid, suppressing the formation of more massive objects. By contrast, the remainder of the IMF is shaped primarily by radiation feedback suppressing fragmentation and preventing small objects from forming, something that appears to happen slightly more efficiently at lower metallicity. The net effect is that the IMF shifts to somewhat lower masses, and is also somewhat narrower, when the metallicity is higher.

While these differences with metallicity provide interesting insight into how feedback interacts with the star-forming environment, they are ultimately of rather minor importance. This is because on an absolute scale the biggest differences we see in the IMF are set by variations in surface density. Our low-surface density cases produce a slightly heavier IMF than our higher surface ones, and the differences are substantially larger than the subtle variations induced by metallicity. When we explore how these IMF variations compare to those required to explain observed variations in the mass-to-light ratio in ETGs compared to spiral galaxies, we find that metallicity-induced IMF changes are too small to explain the observations, whereas surface density-induced ones are at the right level. We therefore conclude that surface density is a more important factor than metallicity in determining the stellar IMF and that the differences observed between the IMFs of spiral and ETGs are most likely an effect of interstellar pressure and therefore surface density, not an effect of metallicity.

ACKNOWLEDGEMENTS

TST and MRK acknowledge support from the Australian Research Council through Laureate Fellowship award FL220100020. This research was undertaken with the assistance of resources and services from the National Computational Infrastructure (NCI), which is supported by the Australian Government, and by resources provided by the Pawsey Supercomputing Research Centre with funding from the Australian Government and the Government of Western Australia.

DATA AVAILABILITY

The data underlying this article will be shared on reasonable request to the corresponding author.

REFERENCES

Bate M. R., 2009, MNRAS, 392, 1363
Bate M. R., 2012, MNRAS, 419, 3115
Bate M. R., 2014, MNRAS, 442, 285
Bate M. R., 2019, MNRAS, 484, 2341
Bate M. R., 2023, MNRAS, 519, 688
Cappellari M. et al., 2012, Nature, 484, 485
Chabrier G., 2005, in Corbelli E., Palla F., Zinnecker H., eds, Astrophysics and Space Science Library, Vol. 327, The Initial Mass Function 50 Years Later. Springer, Dordrecht, p. 41

Chon S., Omukai K., Schneider R., 2021, MNRAS, 508, 4175
Conroy C., van Dokkum P. G., Villaume A., 2017, ApJ, 837, 166
Cunningham A. J., Klein R. I., Krumholz M. R., McKee C. F., 2011, ApJ, 740, 107
Cunningham A. J., Krumholz M. R., McKee C. F., Klein R. I., 2018, MNRAS, 476, 771
da Silva R. L., Fumagalli M., Krumholz M., 2012, ApJ, 745, 145
El-Badry K., Weisz D. R., Quataert E., 2017, MNRAS, 468, 319
Faesi C. M., Lada C. J., Forbrich J., 2018, ApJ, 857, 19
Geha M. et al., 2013, ApJ, 771, 29
Gennaro M. et al., 2018, ApJ, 855, 20
Goldsmith P. F., 2001, ApJ, 557, 736
Gu M., Greene J. E., Newman A. B., Kreisch C., Quenneville M. E., Ma C.-P., Blakeslee J. P., 2022, ApJ, 932, 103
Guszejnov D., Krumholz M. R., Hopkins P. F., 2016, MNRAS, 458, 673
Guszejnov D., Grudić M. Y., Hopkins P. F., Offner S. S. R., Faucher-Giguère C.-A., 2020, MNRAS, 496, 5072
Guszejnov D., Grudić M. Y., Offner S. S. R., Faucher-Giguère C.-A., Hopkins P. F., Rosen A. L., 2022, MNRAS, 515, 4929
Hansen C. E., Klein R. I., McKee C. F., Fisher R. T., 2012, ApJ, 747, 22
Hennebelle P., Chabrier G., 2008, ApJ, 684, 395
Hennebelle P., Chabrier G., 2009, ApJ, 702, 1428
Hennebelle P., Lee Y.-N., Chabrier G., 2019, ApJ, 883, 140
Hopkins P. F., 2012, MNRAS, 423, 2016
Hopkins P. F., 2013, MNRAS, 430, 1653
Jones M. O., Bate M. R., 2018, MNRAS, 478, 2650
Klein R. I., Fisher R. T., McKee C. F., Truelove J. K., 1999, in Miyama S. M., Tomisaka K., Hanawa T., eds, Astrophysics and Space Science Library, Vol. 240, Numerical Astrophysics. Springer, Dordrecht, p. 131
Konigl A., Pudritz R. E., 2000, Protostars and Planets IV. University of Arizona Press, Tucson, p. 759
Krumholz M. R., 2011, ApJ, 743, 110
Krumholz M. R., 2014, Phys. Rep., 539, 49
Krumholz M. R., McKee C. F., Klein R. I., 2004, ApJ, 611, 399
Krumholz M. R., Klein R. I., McKee C. F., 2007, ApJ, 656, 959
Krumholz M. R., Klein R. I., McKee C. F., 2012, ApJ, 754, 71
Krumholz M. R., Fumagalli M., da Silva R. L., Rendahl T., Parra J., 2015, MNRAS, 452, 1447
Krumholz M. R., Myers A. T., Klein R. I., McKee C. F., 2016, MNRAS, 460, 3272
La Barbera F., Ferreras I., Vazdekis A., de la Rosa I. G., de Carvalho R. R., Trevisan M., Falcón-Barroso J., Ricciardelli E. , 2013, MNRAS, 433, 3017
Lee Y.-N., Hennebelle P., 2018, A&A, 611, A89
Li P. S., Martin D. F., Klein R. I., McKee C. F., 2012, ApJ, 745, 139
Li P. et al., 2021, J. Open Source Softw., 6, 3771
Madden S. C. et al., 2013, PASP, 125, 600
Mingozzi M. et al., 2020, A&A, 636, A42
Myers A. T., Krumholz M. R., Klein R. I., McKee C. F., 2011, ApJ, 735, 49
Nam D. G., Federrath C., Krumholz M. R., 2021, MNRAS, 503, 1138
Newman A. B., Smith R. J., Conroy C., Villaume A., van Dokkum P., 2017, ApJ, 845, 157
Offner S. S. R., Klein R. I., McKee C. F., Krumholz M. R., 2009, ApJ, 703, 131
Offner S. S. R., Clark P. C., Hennebelle P., Bastian N., Bate M. R., Hopkins P. F., Moraux E., Whitworth A. P., 2014, in Beuther H., Klessen R. S., Dullemond C. P., Henning T., eds, Protostars and Planets VI. University of Arizona Press, Tucson, p. 53
Oldham L., Auger M., 2018, MNRAS, 474, 4169
Padoan P., Nordlund Å., 2002, ApJ, 576, 870
Padoan P., Nordlund A., Jones B. J. T., 1997, MNRAS, 288, 145
Richer J. S., Shepherd D. S., Cabrit S., Bachiller R., Churchwell E., 2000, in Mannings V., Boss A. P., Russell S. S., eds, Protostars and Planets IV. University of Arizona Press, Tucson, p. 867
Semenov D., Henning T., Helling C., Ilgner M., Sedlmayr E., 2003, A&A, 410, 611
Sharda P., Krumholz M. R., 2022, MNRAS, 509, 1959
Smith R. J., 2020, ARA&A, 58, 577
Spiniello C., Trager S. C., Koopmans L. V. E., Chen Y. P., 2012, ApJ, 753, L32
Spiniello C., Koopmans L. V. E., Trager S. C., Barnabè M., Treu T., Czoske O., Vegetti S., Bolton A., 2015, MNRAS, 452, 2434
Sun J. et al., 2020, ApJ, 901, L8
Tanvir T. S., Krumholz M. R., Federrath C., 2022, MNRAS, 516, 5712
Treu T., Auger M. W., Koopmans L. V. E., Gavazzi R., Marshall P. J., Bolton A. S., 2010, ApJ, 709, 1195
Truelove J. K., Klein R. I., McKee C. F., Holliman J. H. II, Howell L. H., Greenough J. A., Woods D. T., 1998, ApJ, 495, 821
van Dokkum P. G., Conroy C., 2010, Nature, 468, 940

This paper has been typeset from a TEX/LATEX file prepared by the author.